Available online at www.sciencedirect.com

ScienceDirect

Ceramics International 35 (2009) 401–407

CERAMICS INTERNATIONAL

www.elsevier.com/locate/ceramint

Effect of firing temperature and atmosphere on sintering of ceramics made from Bayer process bauxite residue

Y. Pontikes [a], C. Rathossi [c], P. Nikolopoulos [b], G.N. Angelopoulos [a,*], D.D. Jayaseelan [d], W.E. Lee [d]

[a] *Laboratory of Materials and Metallurgy, Department of Chemical Engineering, University of Patras, Rio 26500, Greece*
[b] *Laboratory of Ceramic and Composite Materials, Department of Chemical Engineering, University of Patras, Rio 26500, Greece*
[c] *Section of Earth Materials, Department of Geology, University of Patras, Rio 26500, Greece*
[d] *Department of Materials, Imperial College London, S. Kensington Campus, London SW7 2AZ, UK*

Received 1 October 2007; received in revised form 19 October 2007; accepted 29 November 2007
Available online 10 April 2008

Abstract

Bauxite residue, the principal waste from the Bayer process, was dried, pressed and studied for its thermal and sintering behaviour under different atmospheres, up to 1100 °C. For sintering in air and N_2, shrinkage begins at 800 °C and ranges from 2.6% to 13.9%, after firing at 1000–1100 °C. Bulk density varies from 1.7 to 2.3 g/cm^3 whereas water absorption from 31.5% to 17.7%. The main crystalline phases identified on firing in air were hematite (Fe_2O_3), gehlenite ($Ca_2Al_2SiO_7$) and perovskite ($CaTiO_3$) whereas magnetite (Fe_3O_4) was also found on firing in N_2. Microstructures are characterised by irregularly shaped, <20 μm Feret diameter, pores in a ceramic matrix with interconnected porosity. The average pore size is greater in samples fired in N_2. On sintering in 4%H_2/Ar, shrinkage begins at 710 °C. After firing at 1100 °C, shrinkage is 20.1% and water absorption 1%. The main crystalline phases are magnetite, wustite (FeO), gehlenite and perovskite. Microstructures are characterised by a compact heterogeneous matrix, with isolated <15 μm Feret diameter, closed pores. The grains have reacted with the adjacent phase and their shape is rounded with no sharp facets. Increased sintering temperature results in improved physical properties for all atmospheres tested and in higher average pore size when sintering takes place in air and N_2. The use of magnetite-reducing sintering conditions can potentially assist in the production of a variety of ceramic compositions containing bauxite residue.

Keywords: A. Sintering; Red mud; Bauxite residue; Ceramics; Thermal behaviour

---

1. Introduction

Worldwide, the alumina industry produces approximately 70 Mt/annum of dry Bauxite Residue, BR, (“red mud”) [1]. Typically, BR is considered as a waste being discharged to sea or disposed in ponds or landfills. Only a small fraction of the produced volume is utilized in other industrial processes or applications [2–5]. This relates either to technological limitations of the proposed processes or unfavourable economics, due to the transportation cost in conjunction with the high water content of BR.

In Europe, legislation, public concern and increased awareness of social responsibility from the industrial sector have resulted in intensified efforts towards improved utilization of BR [6]. In this direction, the use of high-pressure filter presses has been industrially implemented in Greece. Efforts are underway for the marketing of the dewatered filter-cake in the cement and heavy clay ceramic industry [3,4] as well as in other applications [7].

Utilization of BR in ceramic production has attracted much interest with more than 55 publications in the last 40 years, ~20% of the scientific output on BR utilization. However, only a few focus on the sintering of 100% BR ceramics. Knight et al. [8] report on the physical–mechanical properties of sintered ceramics from Jamaican BR, prepared from <75 μm powder and sintered at 1000–1100 °C. Apparent porosity was 40–48%, fracture toughness 0.39–0.69 MN/m$^{3/2}$, modulus of rupture 17.23–27.09 MN/m^2, compressive strength 42.0–83.9 MN/m^2 and Brinell Hardness 26.2–59.9 Kg/mm^2. The high strength and toughness achieved is attributed to the formation of a glassy

---

* Corresponding author. Tel.: +302610997509; fax: +302610990917.
E-mail address: angel@chemeng.upatras.gr (G.N. Angelopoulos).

0272-8842/$34.00 © 2008 Elsevier Ltd and Techna Group S.r.l. All rights reserved.
doi:10.1016/j.ceramint.2007.11.013

matrix and is comparable with commercial products. Prasad and Sharma [9], summarizing results on bricks made of 100% BR report that: (a) minimum sintering temperature is 1050 °C and optimum 1100 °C, (b) sintering at >1120 °C leads to dark heavy bricks, deformed and with extensive formation of glassy phase, (c) heating and cooling rates in the range of 10 °C/min are suggested, (d) soaking times of ~100 h seem adequate, and (e) the bricks deteriorate fast. di San Filippo and Usai [10] report that a 100% BR ceramic sintered at 950 °C, achieved compressive strengths similar to those of masonry bricks only when a shaping pressure 5000 kg/m^2 and sintering time >48 h were used. Moya et al. [11], report that sintering of 100% BR ceramics should take place at 1200 °C, where the bodies present the highest shrinkage and minimum water absorption. Finally, Perez et al. [2] also suggest sintering at 1100–1200 °C. To overcome the high shrinkage during sintering, the authors used 74% calcined BR. After sintering at 1175 °C for 4 h, porosity was 12.18% and compressive strength 171.8 MPa, values comparable to commercial heat accumulating bricks.

Despite variations in findings, probably relating to different characteristics of BR and ceramic processing, it is generally accepted that BR demonstrates moderate reactivity when heated in air and up to 1050 °C. Hematite and the developing alumina oxides, accounting usually for more than 50 wt.% of BR, react only to a limited extent, whereas sodium bearing compounds can participate in liquid phase formation. This is further supported by studies on the thermal behaviour of BR [12,13].

Considering the above, it would be beneficial to enhance the reactivity of BR and thus confer added value to the material. This could be done by exploiting the fluxing activity of FeO, where eutectics exist in the SiO_2–CaO–FeO_x, SiO_2–Al_2O_3–FeO_x and Al_2O_3–CaO–FeO_x phase diagrams for ~1100 °C. So far, the use of reducing atmosphere on sintering of BR ceramics has not been investigated. To explore this possibility, the sintering of BR ceramics was studied at temperatures to 1100 °C under different atmospheres.

2. Experimental

BR was supplied by ‘‘Aluminium of Greece’’. The chemical and mineralogical composition is provided in Tables 1 and 2. In terms of particle size distribution, BR is very fine with $d_{10} = 0.7$ μm, $d_{50} = 5.3$ μm and $d_{90} = 74.9$ μm. The material was ground to a particle size <125 μm, mixed with 6 wt.% water and left for 24 h in a hermetically closed plastic bag. Shaping was performed in a uniaxial hydraulic press, at 39 MPa. The samples were cylindrical, 31.0 mm in diameter and 7.5 ± 0.4 mm in height. Drying took place initially at room temperature for 24 h and then in a drying oven at 110 °C till constant weight. After drying, the water content on formation was 5.63 ± 0.34%. The linear shrinkage during drying was minimal. Green density was 1.82 ± 0.05 g/cm^3. Since BR has a specific gravity of 3.4 g/cm^3 this corresponds to ~46% porosity for the green bodies.

Table 1
Chemical composition of BR, wt.%

SiO_2	Al_2O_3	CaO	Fe_2O_3	MgO	K_2O	Na_2O	TiO_2	LOI
7.60	16.63	11.36	42.58	0.56	0.07	3.49	5.00	12.2

Table 2
Mineralogical composition of BR

	Crystalline phases in BR
Major	Hematite Fe_2O_3, diaspore α-AlO(OH), gibbsite γ-$Al(OH)_3$, calcite $CaCO_3$, calcium aluminum iron silicate hydroxide $Ca_3AlFe(SiO_4)(OH)_8$, perovskite $CaTiO_3$, cancrinite $Na_6Ca_2Al_6Si_6O_{24}(CO_3)_2 \cdot 2H_2O$
Minor	Sodium aluminium silicate hydrate $1.0Na_2O \cdot Al_2O_3 \cdot 1.68SiO_2 \cdot 1.73H_2O$, quartz SiO_2, goethite FeO(OH)

Thermal behaviour was studied by dilatometry (402ES, Netzsch) on 25 mm long and 6 mm diameter rods, taken from the cylindrical samples after green machining and polishing with abrasive papers (1200 grit). Maximum sintering temperature was 1000 °C, heating and cooling rates were 5 °C/min and the atmosphere was analytical grade air, N_2 or 4%H_2/Ar at a flow rate of ~1.3 l/h. No soaking time was employed. To assist the interpretation of dimensional changes, BR pellets were fired at selected temperatures in an air-tight, alumina tube resistance furnace, quenched in atmosphere with forced air flow and the crystalline phases were determined by X-ray diffraction analysis, XRD (X-Pert Pro, Philips). The heating rate, atmosphere and flow rate was as in dilatometry experiments. XRD analysis was performed on powdered pellets, for Cu Kα radiation, 40 mA and 40 kV and a 2θ range from 10°–70°.

Based on the dilatometric behaviour and theoretical expectations from ternary phase diagrams, the sintering of BR pellets was studied from 1000 to 1100 °C, with a heating rate of 5 °C/min and 60 min soaking time. Samples were left to cool inside the furnace. The firing and cooling atmosphere was also in this case, analytical grade air, N_2 or 4%H_2/Ar, at a flow rate of ~1.3 l/h.

The physical properties of the sintered bodies were evaluated based on ASTM C373–88 and ASTM C326–82 standard protocols. The crystalline phases were determined by XRD as described above. Pore size distribution was determined by image analysis (SigmaScan Pro, Ver. 4, Jandel Scientific) on backscattered SEM images. The morphology was studied by scanning electron microscopy, SEM, (JSM-6300, Jeol) on gold coated, polished samples. For microchemical analyses, an energy dispersive X-ray spectrometer, EDS (Oxford Instruments), was used. The default standards of LINK ISIS have been used.

3. Results and discussion

Dilatometry, Fig. 1, reveals that to 400 °C, all three atmospheres lead to similar behaviour, i.e. limited dimensional change until 250 °C and then a small contraction until 400 °C. In this temperature interval the reactions taking place correspond to removal of mechanical and crystalline water. At 300 °C, the intensities of calcium aluminum silicate hydroxide peaks are reduced; disappearing completely by 400 °C with a significant

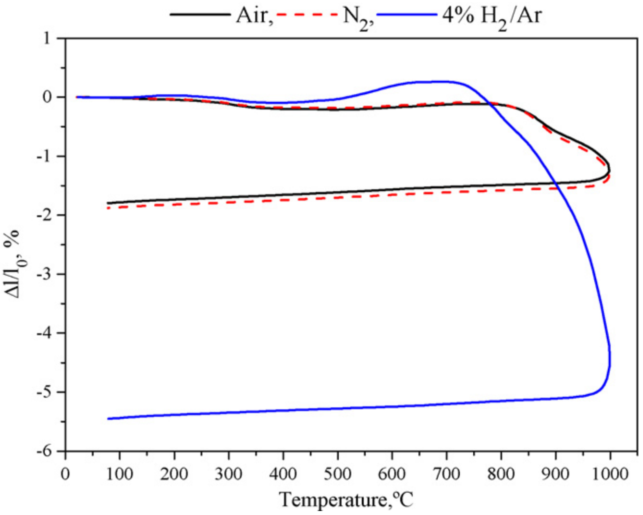

Fig. 1. Dilatometry curves for BR, on sintering in air, N_2 or 4%H_2/Ar, up to 1000 °C. Heating and cooling rate was 5 °C/min.

reduction of gibbsite peaks compared to 300 °C. The transformation of gibbsite will eventually lead to α-alumina (corundum) formation via the hexagonal close packed χ- and κ-alumina or cubic spinel transition phases of γ-, δ- and θ-alumina [14–17]. Nevertheless, the intermediate phases of alumina were not detected by XRD, possibly due to the small extent of their formation and/or poor crystallization. From 400 to 1000 °C, samples sintered in air and N_2 demonstrate comparable behaviour. Up to 800 °C, maximum contraction is only ~0.2% at 500 °C, which coincides with the breakdown of diaspore as revealed by XRD. Corundum derived from diaspore is identified by XRD at >600 °C. The decomposition of calcite initiates at 700 °C and is concluded by 800 °C. In the dilatometry curves there is no dimensional change in this temperature interval and this reflects the two competing phenomena taking place: the thermal expansion in view of the increasing temperature which is offset by the shrinkage after the decomposition of calcite [18]. Shrinkage begins at ~800 °C; for N_2, a slightly higher value is recorded over the air atmosphere at 1000 °C. Reduction of hematite to magnetite, Fe_3O_4, in N_2 initiates at <1000 °C.

Distinctly different behaviour is observed on sintering in 4%H_2/Ar >400 °C. From 400 to 650 °C, an expansion is observed mainly attributed to gas entrapment after the reduction of hematite towards magnetite, which occurs for <500 °C. The slight higher mean volume thermal expansion coefficient of hematite, $23.8 \times 10^{-6}\,K^{-1}$, over that of magnetite, $20.6 \times 10^{-6}\,K^{-1}$ [19], does not obscure the observed trend. As revealed by XRD at 600 °C, the main phases identified were magnetite, hematite, perovskite, calcite and cancrinite, $Na_6Ca_{1.5}Al_6Si_6O_{24}(CO_3)_{1.6}$. Shrinkage begins at 710 °C, ~90 °C lower than in air and N_2 atmospheres. The curve is more abrupt compared to sintering in air and N_2 and the slope is continuously increasing as temperature rises. At 1000 °C, shrinkage was 4.5%.

From 800 to 1000 °C, an array of new phases evolve. At 900 °C, gehlenite, $Ca_2Al_2SiO_7$, is identified by XRD in all samples irrespective of sintering atmosphere. Apart from CaO, Al_2O_3 is also available after the decomposition of gibbsite. The decomposition of diaspore has resulted in α-alumina, which is expected to be less reactive. This is corroborated by the XRD peaks of α-alumina that are little affected from 700 to 1100 °C. The formation of gehlenite is most likely controlled by the availability of quartz, which exists in a limited amount in the raw material. Another potential route for gehlenite formation would be through $Ca_3Al_2(SiO_4)(OH)_8$. At 1000 °C, nepheline, $NaAlSiO_4$, is also identified by XRD for all atmospheres tested. A possible route of formation is through the decomposition of cancrinite ($Na_6Ca_{1.5}Al_6Si_6O_{24}(CO_3)_{1.6}$) towards $NaAlSiO_4$, CaO and CO_2. Indeed, cancrinite's XRD reflections remain to 900 °C and disappear at 1000 °C, consistent with Ishmael [20] who reported loss of the supercell at 868 °C and maximum loss of CO_2 at 949 °C, and similar to other studies of BR [12]. This reaction provides additional CaO to the system which can further react. In the sample fired in air, sodium aluminum silicate $Na_6(AlSiO_4)_6$ was also identified by XRD. Its formation could result after sodium aluminum silicate hydrate ($1.0Na_2O{\cdot}Al_2O_3{\cdot}1.68SiO_2{\cdot}1.73H_2O$) which was originally present in BR.

The presence of calcium aluminum oxide, $CaAl_2O_4$, also found by others [12], is consistent with most XRD spectra and is likely in view of the availability of CaO and Al_2O_3. However, there is major peak overlap between hematite, perovskite and calcium aluminum oxide and its presence cannot be confirmed. Quartz, although not detected by XRD above 600 °C, was identified by SEM-EDX. Perovskite is also present in all conditions examined and remains practically inert.

On cooling, the dimensional change with temperature is practically constant for all conditions tested. The overall shrinkage was 1.8–1.9% for sintering in air and N_2, and ~5.5% for sintering in 4%H_2/Ar. Sintering in air results in red/brown bodies while in N_2 or 4%H_2/Ar the bodies become dark grey/black.

In Fig. 2, linear shrinkage and water absorption is presented. Results for sintering in air and N_2 are comparable for all temperatures and atmospheres studied. For sintering at 1000 °C, shrinkage in air and N_2 atmosphere is ~2% whereas for 4%H_2/Ar it increases to ~8%. The values for air and N_2 are slightly higher than those recorded in dilatometry; for 4%H_2/Ar the difference is substantial (8% against 5.5% in dilatometry). This effect reflects the role of the isothermal step in the soaking zone which is influential for body densification in 4%H_2/Ar and of limited importance in air and N_2. As sintering temperature rises, shrinkage increases for all three atmospheres tested and becomes highly dependant on sintering temperature in 4%H_2/Ar atmosphere. For 1100 °C, shrinkage on sintering in air and N_2 is ~10% whereas for 4%H_2/Ar it approaches 21%.

Water absorption shows inverse behaviour to shrinkage with sintering temperature and decreases as temperature rises. The results for sintering in air and N_2 are similar. In the case of 4%H_2/Ar values are considerably reduced. Best results were obtained for the maximum sintering temperature in each case: for sintering in air and N_2, water absorption was ~18% and for 4%H_2/Ar, ~1%.

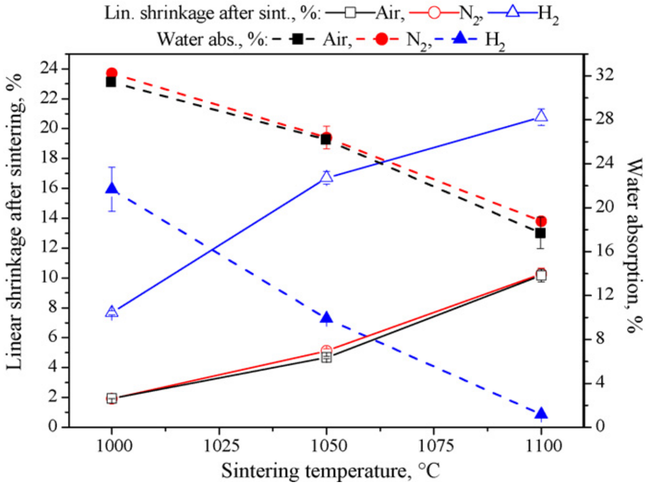

Fig. 2. Linear shrinkage and water absorption of the sintered bodies with respect to sintering temperature and atmosphere.

Fig. 3 shows changes in bulk density and weight loss with sintering atmosphere and temperature. For 1000 °C, the values for bulk density are comparable being ∼1.7 g/cm^3 for sintering in air or N_2, and ∼2.0 g/cm^3 for 4%H_2/Ar. For the highest sintering temperature, bulk density increases to 2.3 and ∼3.3 g/cm^3 for sintering in air or N_2 and 4%H_2/Ar, respectively.

Weight loss on sintering is consistent with the reduction potential of the three atmospheres tested and increases as sintering temperature rises. Based on stoichiometric calculations, presented elsewhere [21], and on the fact that no hematite reduction was detected on sintering in air below 1100 °C, a semi-quantitative calculation of hematite reduction is possible. The reaction path involves hematite reduction to magnetite as a first stage, with a weight loss of 3.33%, and magnetite reduction to wustite, FeO, as a second stage, with a weight loss of 6.91%. Based on the above and assuming the absence of other reactions affecting the mass of the samples, sintering at 1000 °C in N_2 results in ∼50 wt.% Fe_2O_3 and ∼50 wt.% Fe_3O_4 whereas for the same temperature but 4%H_2/Ar atmosphere, the iron oxides are ∼67 wt.% Fe_3O_4 and ∼33 wt.% FeO. Obviously, the iron oxides may have reacted with crystalline or glassy phases and therefore need not be these oxides in the sintered body. For samples sintered in N_2, the higher weight loss compared to sintering in air was not accompanied by higher shrinkage or reduced open porosity. The most plausible explanation lays in

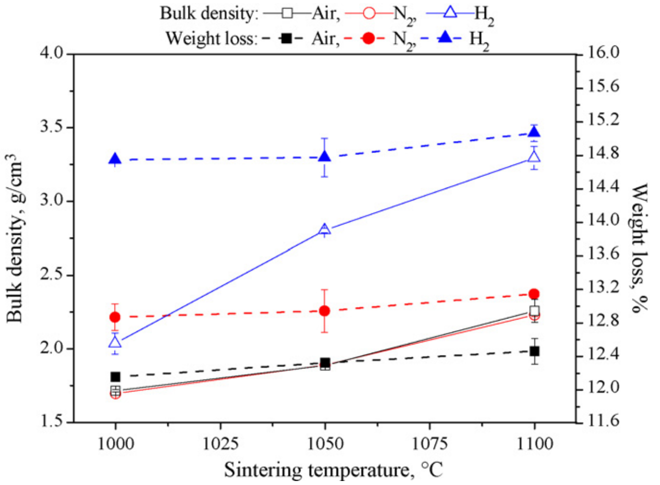

Fig. 3. Bulk density and weight loss of the sintered bodies with respect to sintering temperature and atmosphere.

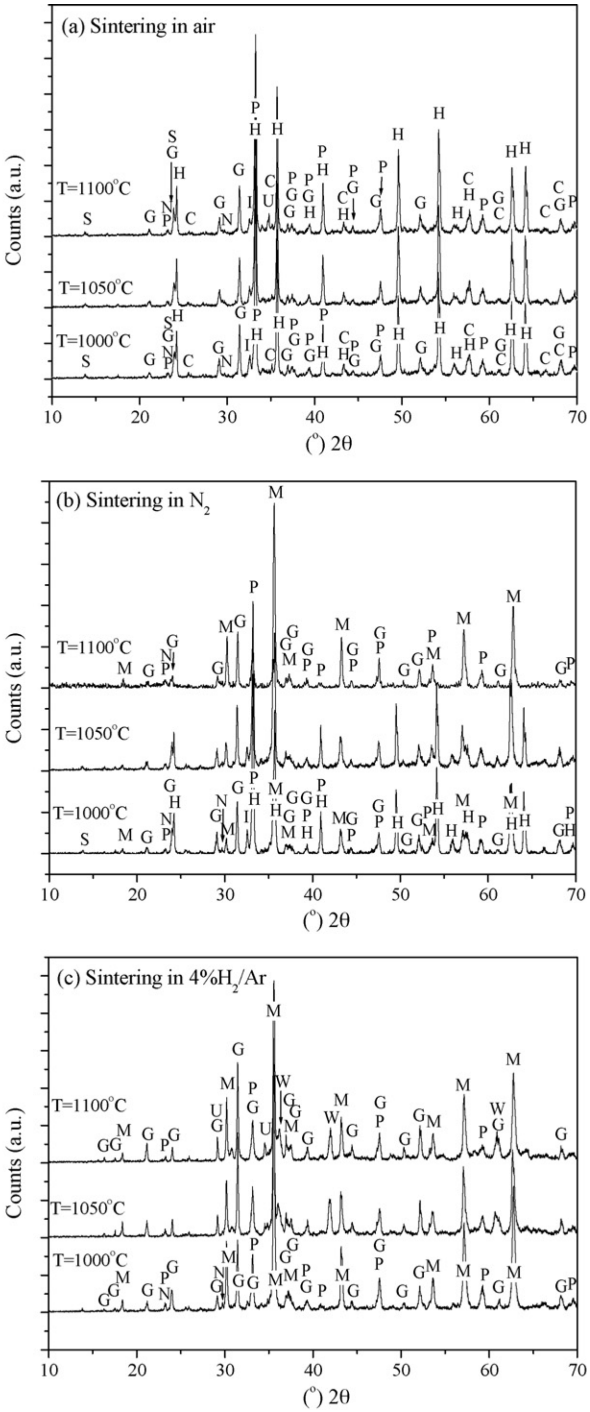

Fig. 4. XRD after sintering at 1000, 1050 and 1100 °C in (a) air, (b) N_2 and (c) 4%H_2/Ar. H: hematite Fe_2O_3, M: magnetite Fe_3O_4, W: wustite FeO, P: perovskite $CaTiO_3$, G: gehlenite $Ca_2Al_2SiO_7$, C: corundum Al_2O_3, N: nepheline $NaAlSiO_4$, S: sodium aluminum silicate $Na_6(AlSiO_4)_6$, I: ilmenite $FeTiO_3$, and U: ulvospinel Fe_2TiO_4.

considering a higher development of closed porosity in the case of N_2 as corroborated by SEM observations.

In Fig. 4, the XRD spectra of samples sintered in the interval 1000–1100 °C are presented. For sintering at 1000 °C in air, the main phases identified were hematite, perovskite, gehlenite, nepheline, corundum, sodium aluminum silicate and ilmenite, $FeTiO_3$. At 1050 °C, the same crystalline phases are present whereas at 1100 °C, ulvospinel, Fe_2TiO_4, is also present, most likely formed after the reaction of hematite and ilmenite with concurrent release of oxygen.

Sintering in N_2 at 1000 and 1050 °C results in a two-zone microstructure. In the outer part, a black rim is formed where magnetite is the only iron oxide present. The thickness of the rim is typically less than 1800 μm, depending on the sintering temperature. In the core of the body, hematite prevails giving a distinct red colouration. This effect is due to limited H_2 penetration into the interior of the body and is frequently encountered in hematite-reducing sintering [22,23]. At 1000 °C the main phases recorded for the whole of the body were hematite, magnetite, perovskite, gehlenite, nepheline and corundum. At 1050 °C, qualitatively the same phases are present as for sintering at 1000 °C with a higher ratio of magnetite to hematite. At 1100 °C only magnetite is present, the other phases being perovskite, gehlenite, nepheline and corundum.

After sintering in 4%H_2/Ar, the section of the body appears homogeneous. Probably this relates to the early hematite

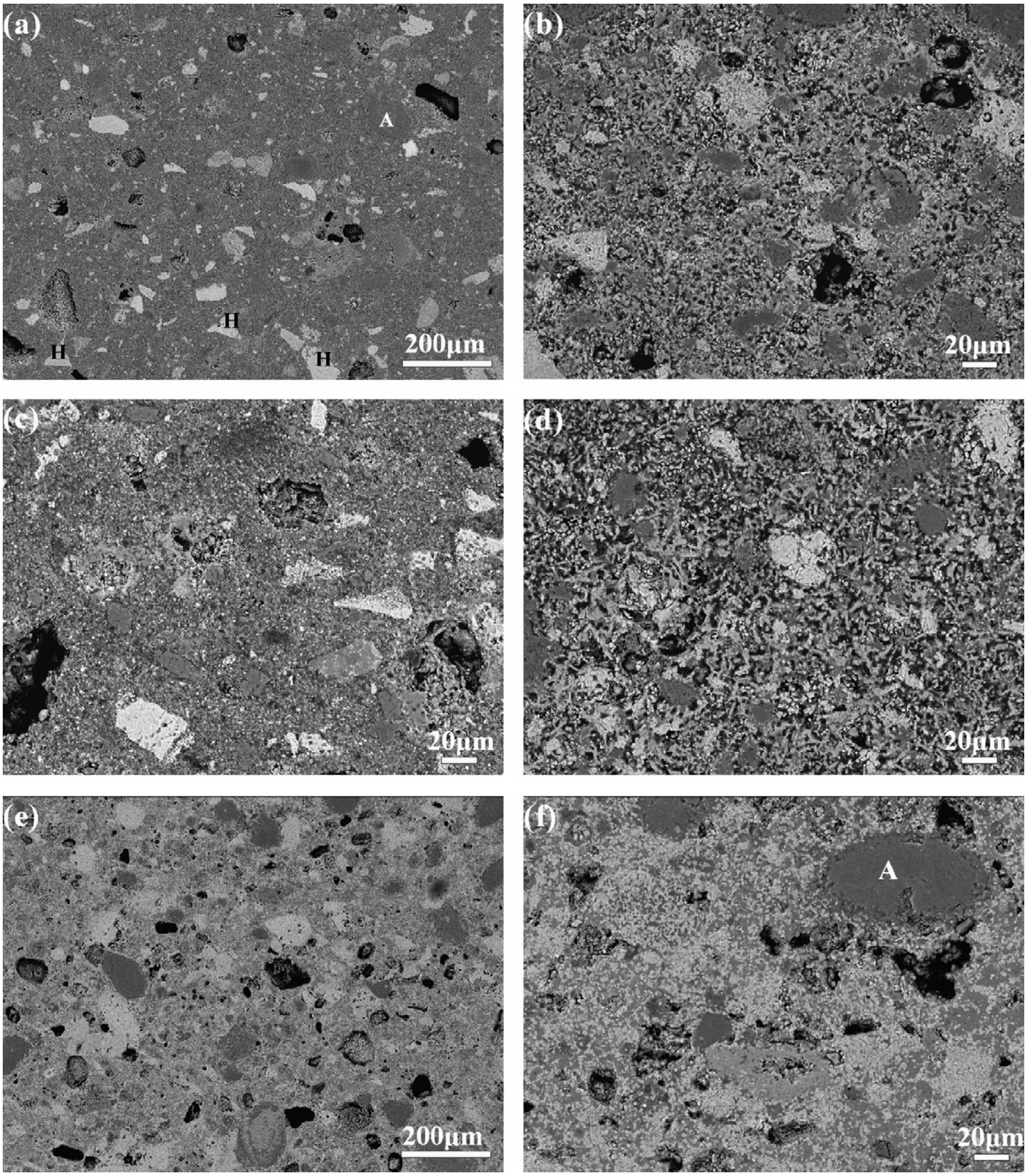

Fig. 5. Backscattered electron images of polished surfaces after sintering in (a) air at 1000 °C, (b) air at 1100 °C, (c) N_2 at 1000 °C. (d) N_2 at 1100 °C, (e) 4%H_2/Ar at 1100 °C, and (f) 4%H_2/Ar at 1100 °C. H: hematite, A: aluminum oxide.

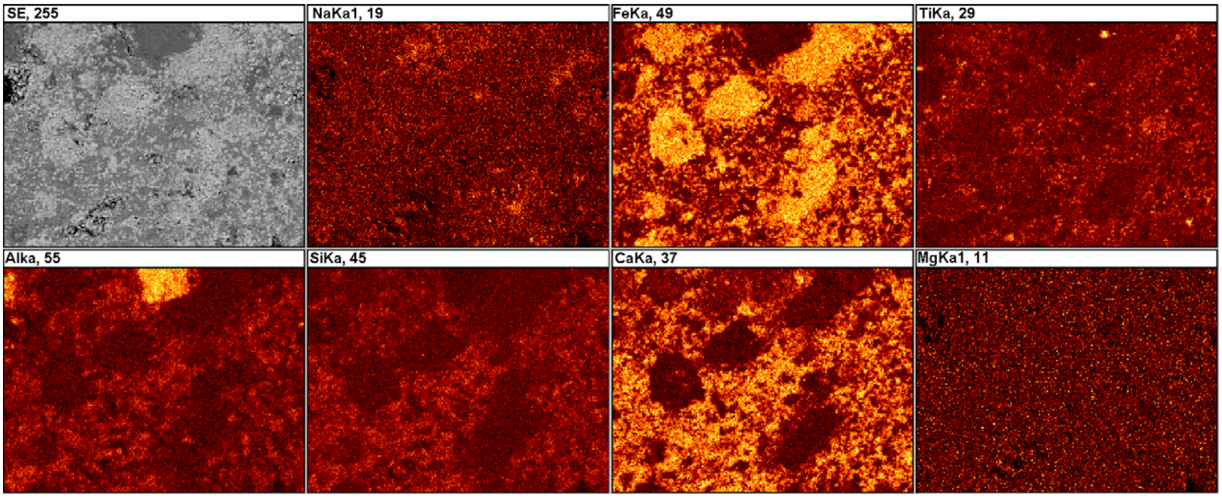

Fig. 6. Elemental mapping on polished surface after sintering in 4%H_2/Ar, at 1100 °C. Top row, left to right: secondary electron image of the surface and map of Na, Fe and Ti, respectively. Bottom row, left to right: map of Al, Si, Ca and Mg, respectively.

reduction at <600 °C, where porosity is predominantly open and gas permeability more effective. At 1000 °C, magnetite, perovskite, gehlenite, nepheline and corundum were the main phases detected. At 1050 °C nepheline peak intensities are reduced and wustite crystallises, the other phases presenting minor fluctuations in their characteristic peaks. At 1100 °C, magnetite, wustite, perovskite, gehlenite corundum and ulvospinel were detected; nepheline is no longer present.

After sintering in air at 1000 °C, Fig. 5(a), microstructures are characterised by large, <60 μm Feret diameter, alumina and hematite grains surrounded by a microcrystalline matrix. The large grain morphologies reveal limited reaction with the adjacent material since they retain the original angular shape. Porosity is interlinked with large pores, <20 μm Feret diameter, in a matrix of submicron pores. After sintering at 1100 °C, Fig. 5(b), smaller pores remain predominantly interconnected although they coalesce leading to a higher mean pore size. Large pores remain and the grain morphology changes little from that after sintering at 1000 °C.

Sintering in N_2 at 1000 °C, Fig. 5(c), leads to a texture comparable to that for sintering in air. However, at the highest temperature, Fig. 5(d), grains have reacted more extensively and porosity is of greater mean size. Typically, also in this case, porosity is interconnected creating an open cellular structure. Nonetheless, closed pores are visible and in addition highly compact areas are present where open porosity is minimal.

After sintering in 4%H_2/Ar at 1000 °C, the microstructure is characterised by a distinctly reduced open porosity. A dense mass surrounds the grains of the microstructure. The different contrast in backscattered electron images as well as EDS analyses reveal a variation in the microchemical analysis of this mass. Efforts to establish a SiO_2/Al_2O_3 or $SiO_2 + Al_2O_3 + TiO_2/Na_2O + K_2O + CaO + MgO + FeO$ ratio were met with limited success. For the highest sintering temperature, the microstructure is different from all previous cases. Larger pores are rounded and reduced in size, typically <15 μm Feret diameter, Fig. 5(e). Submicron porosity is limited. Alumina grains have formed a reaction rim on the interface, Fig. 5(f). Iron oxide grains have dissolved in the adjacent matrix, which also in this case is inhomogeneous. This is apparent in the elemental mapping of Fig. 6. Iron oxide grains are still present; however, their characteristic conchoidal shape is lost. On the contrary, alumina grains have retained to a greater extent the original morphology. Concerning the other elements, Ti is locally present in crystals of rutile (although not detected by XRD) and perovskite, whereas Ca, at a higher concentration, and Si, at a lower, are widespread in the matrix. Na and Mg are minor constituents and do not reveal any pattern of presence. Finally, on some occasions Na-rich water soluble salts crystallise on the surface, with flower-like morphology.

4. Conclusions

Sintering of BR ceramics in air or N_2 results in similar dilatometric behaviour and comparable physical properties, crystalline phases and microstructure. On the other hand, when sintering takes place in 4%H_2/Ar, shrinkage initiates at a lower temperature and results in a highly densified body. Generalising, the three main oxides of BR can be viewed as components of a triaxial system: iron oxides function either as a filler (hematite, magnetite) or as a flux (wustite), alumina oxides as fillers (minimum dissolution) and calcium oxide as mineraliser (reacting mainly towards gehlenite).

The above results demonstrate that use of magnetite-reducing sintering conditions can potentially assist in the production of a variety of compositions with BR. This would be challenging for the body formulation and sintering profile design, where a balance will have to be attained between uniform reduction of iron oxides, control of shrinkage during sintering and regulation of the amount and viscosity of the liquid phase generated.

Acknowledgements

The authors from Univ. of Patras acknowledge the financial support provided by the “ΕΠΑΝ” project No. 12252/19–11–02.

The contribution of T. Bergara and A. Marie, ENSIACET, National Polytechnic Institute of Toulouse, France, within the framework of Erasmus project, is gratefully acknowledged.

References

[1] The Aluminum Association, Technology Roadmap for Bauxite Residue Treatment and Utilization, 2000, The Aluminum Association.

[2] R.G.A. Perez, R.F. Guitian, S. De Aza Pendas, Industrial obtaining of ceramic materials from the Bayer process red mud's, Bol. Soc. Esp. Ceram. V 38 (3) (1999) 220–226.

[3] T. Brown, J. Beretka, Red mud as a raw material for the heavy clay industry, Ceramurgia 14 (4) (1984) 155–160.

[4] R. Bott, T. Langeloh, J. Hahn, Re-usage of dry bauxite residue, in: Proc. 7th Int. Alumina Quality Workshop, Perth Australia, (2005), pp. 236–241.

[5] R.K. Paramguru, P.C. Rath, V.N. Misra, Trends in red mud utilization—a review, Miner. Process. Extr. M. 26 (2005) 1–29.

[6] W.E. Lee, A.R. Boccaccini, J.A. Labrincha, C. Leonelli, C.H. Drummond III, C.R. Cheeseman, Green engineering: ceramic technology and sustainable development, Bull. Am. Ceram. Soc. 86 (2) (2007) 18–25.

[7] D. Boufounos, Alternative applications for bauxite residue, in: Proc. 1st Hellenic Conf. for the Utilization of By-Products in Construction, Thessaloniki, (2005), pp. 183–190.

[8] J.C. Knight, A.S. Wagh, W.A. Reid, The mechanical properties of ceramics from bauxite waste, J. Mater. Sci. 21 (6) (1986) 2179–2184.

[9] P.M. Prasad, J.M. Sharma, Characterization of and applications for an Indian red mud, Proc. Electrometallurgy (1986) 12–23.

[10] P.A. di San Filippo, G. Usai, The recycling of red mud from the Bayer Process, part 1, production of masonry bricks at a firing temperature of 950 °C, ZI, Ziegelindustrie Int. 41 (2–3) (1988) 67–74.

[11] J.S. Moya, F. Morales, V.A. Garcia, Ceramic use of red mud from alumina plants, Bol. Soc. Esp. Ceram. V 26 (1) (1987) 21–29.

[12] V.M. Sglavo, R. Campostrini, S. Maurina, G. Carturan, M. Monagheddu, G. Budroni, G. Cocco, Bauxite "red mud" in the ceramic industry. Part 1: thermal behaviour, J. Eur. Ceram. Soc. 20 (3) (2000) 235–244.

[13] S. Srikanth, A.K. Ray, A. Bandopadhyay, B. Ravikumar, J. Animesh, Phase constitution during sintering of red mud and red mud-fly ash mixtures, J. Am. Ceram. Soc. 88 (9) (2005) 2396–2401.

[14] K.J.D. MacKenzie, J. Temuujin, K. Okada, Thermal decomposition of mechanically activated gibbsite, Thermochim. Acta 327 (1999) 103–108.

[15] I. Levin, D. Brandon, Metastable alumina polymorphs: crystal structures and transition sequences, J. Am. Ceram. Soc. 81 (8) (1998) 1995–2012.

[16] A. Atasoy, An investigation on characterization and thermal analysis of the Auginish red mud, J. Therm. Anal. Calorim. 81 (2005) 357–361.

[17] J.T. Kloprogge, H.D. Ruan, R.L. Frost, Thermal decomposition of bauxite minerals: infrared emission spectroscopy of gibbsite, boehmite and diaspore, J. Mater. Sci. 37 (6) (2002) 1121–1129.

[18] K. Feng, S. Lombardo, Kinetic analysis from dilatometry and mass spectrometry measurements of the decomposition and sintering of calcium carbonate, J. Ceram. Process. Res. 3 (3) (2002) 101–108.

[19] B.J. Skinner, in: S.P.J. Clark (Ed.), Handbook of Physical Constants, Thermal Expansion, Geol. Soc. Am. Mem., 1966, pp. 75–95.

[20] H. Ishmael, The thermal behavior of cancrinite, Can. Miner. 34 (4) (1996) 893–900.

[21] L. Piga, F. Pochetti, L. Stoppa, Application of thermal analysis techniques to a sample of red mud—a by-product of the Bayer process—for magnetic separation, Thermochim. Acta 254 (1995) 337–345.

[22] J.E. Houseman, C.J. Koenig, Influence of kiln atmospheres in firing structural clay products: I, maturation and technological properties, J. Am. Ceram. Soc. 54 (2) (1971) 75–82.

[23] J.E. Houseman, C.J. Koenig, Influence of kiln atmospheres in firing structural clay products: II, color development and burnout, J. Am. Ceram. Soc. 54 (2) (1971) 82–89.